World Conference on Timber Engineering Oslo 2023

PENDULUM IMPACT HAMMER TESTS ON TIMBER BEAMS – EXPERIMENTAL SETUP

Alex Sixie Cao[1], Andrea Frangi[2]

ABSTRACT: In this paper, a test setup for conducting impact testing of full-size timber beams is presented. The test setup comprises a pendulum impact hammer with an effective length of 4750 mm, mass of 3475 kg, and can be released from a near-horizontal position. On the impact hammer, 100g accelerometers and a shock-resistant high-speed camera with a capacity of up to 5700 pictures per second were installed. In addition, other cameras were installed, as well as an angular encoder to record the position of the pendulum impact hammer. The pendulum impact hammer was released using an electromechanical release system attached to a crane. The impact hammer was designed for impact tests on timber beam specimens with cross-sections ranging from 160x160 mm to 200x320 mm and lengths between 2700 and 4300 mm. The results include the energy release of the specimens upon failure, peak impact forces, time to failure, and high-speed imagery. With the test setup, similar knowledge can be gained for other engineered wood products.

KEYWORDS: Glued laminated timber, Impact loading, Pendulum impact hammer, Full-size tests

1 INTRODUCTION

In recent years, the popularity and use of timber as a structural material for tall buildings and bridges has increased [1,2] as the drive for sustainability continues. Because of the growing volume of structural timber in our built environment, structural robustness and disproportionate collapse prevention [3–7] is receiving renewed attention from timber engineers worldwide as timber buildings reach record heights with recent technological developments [3,8–15].

To assess the collapse behaviour and resistance of timber buildings, advanced numerical models are needed [4]. An important feature of the numerical models is the ability to simulate member failure and separation from rapid loading [3,14,15]. The rapid loading may stem from impact loading from vehicles, falling debris, projectiles, explosion debris, blast loading, and more.

Previous impact tests on wood or timber were conducted on 10 to 20 mm square small clearwood [16], 50 to 150 mm square lumber [17,18], and single boards [19–21] using either a small pendulum impact hammer or a drop test. However, the size effects in timber are considerable because of the natural growth imperfections in wood such as knots, distorted grains, and more [22,23]. In addition, the results from single boards cannot be generalised to glued assemblies, such as glued laminated timber (GLT) or laminated veneer lumber (LVL). Thus, it is necessary to conduct full-size impact tests on engineered wood products commonly used in practice.

Timber is known to be rate-dependent, which is reflected in the current set of design codes in Europe [24,25]. However, the shortest codified loading duration is in the order of seconds, which is not valid for impact loading, where the loading occurs within milliseconds [26].

To address these challenges, pendulum impact hammer tests were conducted on 86 full-size spruce GLT specimens without finger joints and nine full-size beech laminated veneer lumber specimens. The cross-sections were between 160×160 and 200×320 mm, and the lengths between 2700 and 4300 mm. The test setup was instrumented with accelerometers, angular encoders, and high-speed cameras. The effective length of the impact hammer was about 4750 mm, with a mass of 3450 kg.

In this paper, the conceptual framework and the most important aspects of the test setup are presented.

Data from the sensors are shown, as well as images from a high-speed camera. The full results of the experimental campaign are published in a test report [27]. The bespoke test setup was designed and built at ETH Zurich.

2 THEORETICAL FRAMEWORK

2.1 PENDULUM IMPACT HAMMER

A pendulum impact hammer setup was chosen because of the possibility of a direct measurement of the energy release E_r from the failure of a specimen. In such a setup, the energy balance can be written as:

$$m_p g h_0 = m_p g h_1 + E_r + E_c, \quad (1)$$

where m_p is the effective mass of the impact hammer, g=9.806 m/s^2 is the gravitational acceleration in Zurich, h_0 is the initial height of the impact hammer, h_1 is the post-impact height of the impact hammer, E_r is the energy release from the failure of the specimen, and E_c are other sources of energy loss, such as friction and drag. The

[1] Alex Sixie Cao, Institute of Structural Engineering, ETH Zurich, 8092 Zurich, Switzerland, cao@ibk.baug.ethz.ch
[2] Andrea Frangi, Institute of Structural Engineering, ETH Zurich, 8092 Zurich, Switzerland, frangi@ibk.baug.ethz.ch

https://doi.org/10.52202/069179-0002

concept of the pendulum impact hammer setup is shown in Figure 1, where L_{CM} is the length from the point of rotation to the centre of mass of the impact hammer, and θ_i are the initial and post-impact angles of the impact hammer. The energy release E_r can be used to find the peak dynamic impact force P_d and to quantify the toughness U_T of the tested material [28].

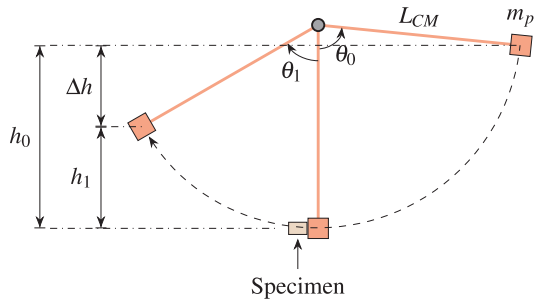

Figure 1: *Conceptual framework of the tests. The figure is reproduced from Cao et al.* [28].

2.2 PEAK IMPACT FORCE

To compare the energy release E_r in Equation (1) of different specimens or materials, it can be normalised with respect to the cross-sectional area A of the specimen:

$$U_T = \frac{E_r}{A}. \tag{2}$$

U_T in Equation (2) is defined as the toughness of the material. By assuming that the specimen can be idealised as an Euler-Bernoulli beam without shear deformations, and the load-displacement behaviour as linear-elastic perfectly brittle, the peak impact force P_d can be found by considering the equivalent single-degree-of-freedom system in Figure 3. In Figure 3, v_p is the impact velocity, U is the strain energy, U^* is the complementary strain energy, w is the mid-span deflection, and $k=48EI/L^3$ is the equivalent stiffness.

Since the load-displacement curve is linear-elastic perfectly brittle, the strain energy U is the same as the complementary strain energy U^*. The energy release E_r is the same as the strain energy U or the complementary strain energy U^*. Therefore, the peak impact force P_d can be found by considering the triangular area above the load-displacement curve:

$$E_r = \frac{1}{2}\frac{P_d^2}{k} \therefore P_d = \sqrt{2E_r k} = \sqrt{E_r \frac{96EI}{L^3}}, \tag{3}$$

where L is the length, E is the elastic modulus, and I is the second moment of area of the specimen. Equation (3) can also be found by following a strain energy approach.

If the collision between the impact hammer and the specimen is considered as perfectly inelastic until failure, the peak impact force P_d can be found by considering the deceleration a of the impact hammer. With Newton's second law, the peak impact force P_d can be expressed as:

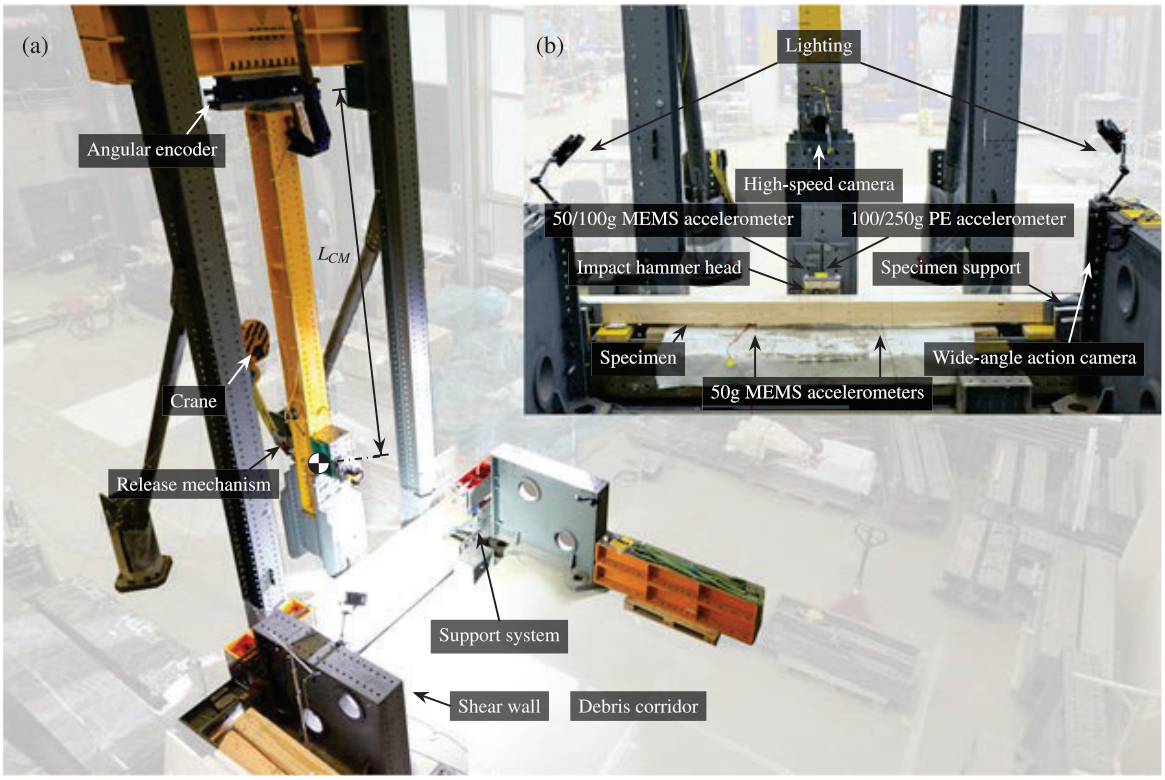

Figure 2: *Experimental setup, where PE denotes piezoelectric, and MEMS micro-electromechanical system. (a) Bird's-eye view; and (b) front view of the test setup. The figure is reproduced from Cao et al.* [28].

https://doi.org/10.52202/069179-0002

$$P_d = m_p a. \quad (4)$$

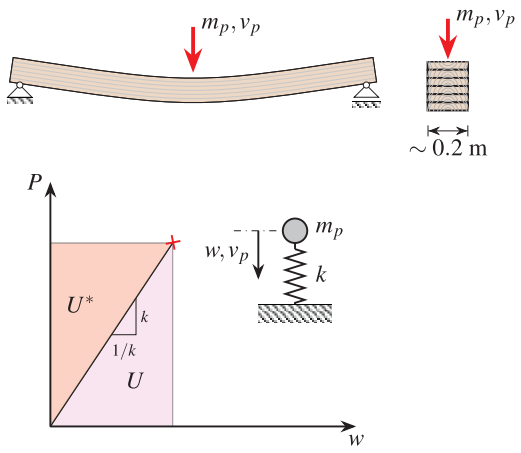

Figure 3: *Single-degree-of-freedom idealisation of a simply supported beam loaded at the mid-span. The figure is reproduced from Cao et al.* [28].

3 EXPERIMENTAL SETUP

3.1 PENDULUM IMPACT HAMMER

The test setup was designed using the computer-aided-design software Autodesk Inventor to accommodate simply supported specimens with and without axial restraints of dimensions between 160×160×2900 mm and 200×320×4300 mm. Because of the limited available information on the expected energy release E_r of the specimens, the energy capacity mgh_0 of the impact hammer setup was maximised. The length h_0 was constrained by the physically available space in the laboratory at ETH Zurich, and the mass m by the steel plates in the laboratory inventory. The effective length L_{CM} of the impact hammer became 4650 mm, and the mass was 3475 kg. The impact hammer could be raised to a maximum angle of about 87°, which results in a maximum potential energy mgh_0 of about 158 kJ.

To support the impact hammer, an S355 steel frame comprising two IPE 360×7040 mm columns and two stacked and bolted HEB 300×2050 mm beams was used, where the impact hammer was suspended from the HEB 300×2050 beams. To provide lateral stiffness to the frame in the pendulum's direction of motion, two ROR 159×25×4000 mm diagonal trusses were bolted to the IPE 360×7040 mm columns. The frame and the diagonal trusses were fixed to a strong floor using two M55 10.9 steel bolts for each steel footing, post-tensioned to 1000 kN. Most of the bolts were M24 8.8, with a few M16 8.8 bolts used in the shear pin. The experimental setup is shown in Figure 2.

3.1.1 SHEAR PIN & HINGE SYSTEM

The impact hammer was suspended from the two HEB 300×2050 mm beams via an elaborate hinge system. The hinge system comprised a Ø40×1210 mm 10.8 steel shear pin with a hardened surface, four double hinges, five single hinges, and various S355 adapter plates. In addition, steel tubes were attached at the ends of the shear pin to prevent the shear pin from sliding out of the hinges. This is shown in Figure 4.

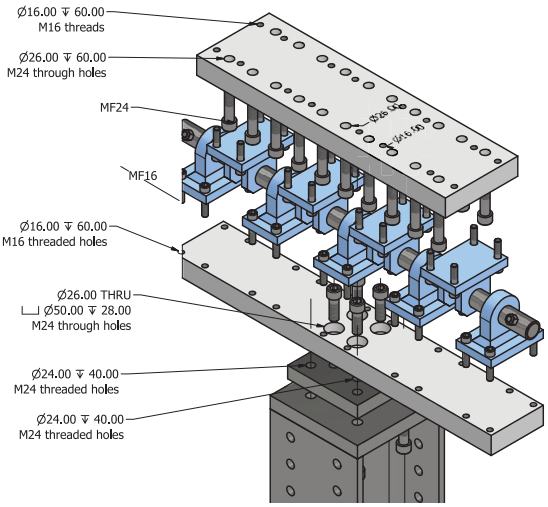

Figure 4: *Shear pin and hinge system, which connects the impact hammer to the pendulum frame. The figure is reproduced from Cao et al.* [27].

The shear pin was designed as a beam with a circular cross-section subjected to equidistant point loading on the characteristic material strength level. Since the hinges were standard inventory in the laboratory, the cross-section of the shear pin was fixed. Therefore, the design was focused on the necessary number of hinges to satisfy von Mises stresses on the characteristic level, as well as an L/400 maximum deflection criterion. The system was designed against a maximum shear force of 1000 kN, in combination with a 100 kN centrifugal force. The maximum allowable deflection was the governing design criterion. The thicknesses of the adapter plates were governed by the minimum thread length of the M24 bolts.

3.1.2 SPECIMEN SUPPORTS

The specimen ends were placed in steel brackets, which were bolted to rotation hinges. The hinges provided the simply supported support conditions. To enforce axial restraints, the specimens could be fixed to the steel brackets using glued-in or threaded rods. This is shown in Figure 5. In Figure 5a, the screws were mounted for transportation and were removed before testing.

To account for uncertainties in the specimen lengths and other parts of the setup, a sliding system with several centimetres of adjustability was designed. The sliding system comprised a steel plate with long holes, which was bolted to a shear wall. The reaction forces were transferred to the strong floor through the shear walls, which were connected to the pendulum frame via two connected HEB 300 mm beams. This is shown in Figure 6. To accommodate different specimen lengths, the shear walls could be moved with rough precision, and the steel plate with the long holes provided exact precision.

https://doi.org/10.52202/069179-0002

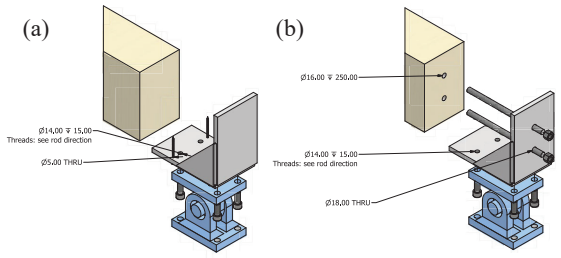

Figure 5: *Steel brackets with simply supported boundary conditions (a) without axial restraints, and (b) with axial restraints. The figure is reproduced from Cao et al.* [27].

For the axially unrestrained specimens, the halves of the specimens would fly out of the steel brackets in the direction of the impact hammer motion. However, this was not the case for the axially restrained specimens. Because of the axial restraints, the two halves were kept in the steel brackets by the glued-in rods. To prevent a reverse impact by the impact hammer on its return to the side of the initial release, a recoil control system was implemented for safety reasons. The recoil system comprised a pair of steel rods, which were released vertically after the first impact. This prevented the halves of the specimen from returning to its initial position, ensuring a gap that the impact hammer could return through. This is shown in Figure 7.

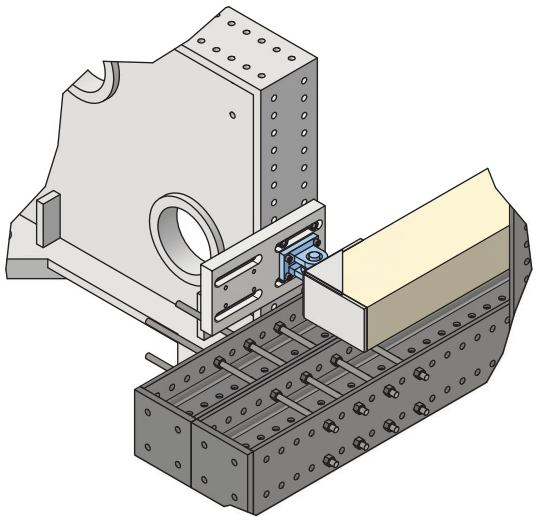

Figure 6: *Specimen support system. The figure is reproduced from Cao et al.* [27].

3.1.3 IMPACT HAMMER HEAD

The head of the impact hammer comprised steel plates of various dimensions to ensure a sufficient mass of the impact hammer. The steel plates were post-tensioned using M24 and M16 8.8 threaded rods. To provide a clean impact surface, a 300×350×70 mm S355 steel plate with rounded edges was machined and mounted at the tip of the impact hammer head. The effective contact surface between the impact hammer tip and the specimen was 250×200 mm. The total mass of the impact hammer head

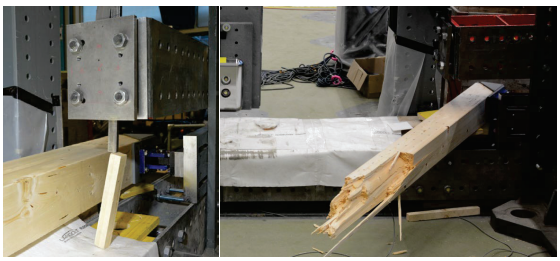

(a) Activated rods. (b) Rods post-release.

Figure 7: *Recoil system for the axially restrained specimens. The figure is adapted from Cao et al.* [27].

was about 2736 kg. The total mass of the impact hammer, including instrumentation, was approximately 3475 kg, with a centre of mass from the shear pin of 4649 mm. The impact hammer head is shown in Figure 2b, and the impact hammer tip in Figure 8.

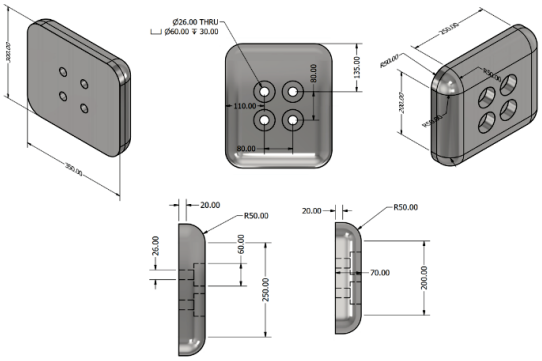

Figure 8: *Impact hammer tip. The figure is reproduced from Cao et al.* [27].

3.1.4 RELEASE SYSTEM

A crane was used to lift the impact hammer to its release height and an electromechanical release mechanism was used to release the impact hammer. This is shown in Figure 2a. Because the loading capacity of the electromechanical release mechanism was limited to 2500 kg, a load reduction system was necessary to reduce the weight $m_p g$ of the impact hammer on the electromechanical release mechanism.

The load reduction system comprised steel shackles, lifting slings, and a dynamic climbing rope. These parts were organised in a pulley system, such that the final load on the electromechanical release mechanism was reduced to $m_p g/6$. The load reduction system is illustrated in Figure 9. A dynamic climbing rope was preferred over steel cables or static ropes because of its ability to damp out vibrations and its flexibility and adjustability. The dynamic climbing ropes had a total length of approximately 1.6 m and were inspected after each test. Unless damage was detected during the visual inspection, they were used four to six times before being replaced. Figure of eight knots were tied at each end of the ropes, which is a standard knot used in sports climbing.

Once the release mechanism was triggered, the dynamic climbing rope would unloop itself from the shackles and remain on the crane. The induced energy loss from the

https://doi.org/10.52202/069179-0002

unlooping action was corrected for in the tests by comparing the energy loss between subsequent harmonic oscillations. This is described in Section 4.2.

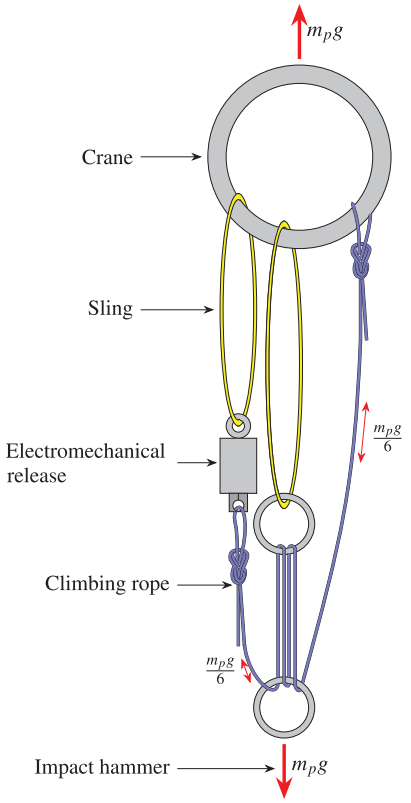

Figure 9: *Release and load reduction system of the impact hammer.*

3.2 CAMERAS AND SENSORS

To capture the impact and failure process of the specimen, several cameras were used. The main camera was an AOS M-VIT 4000 shock-resistant high-speed camera operating at 5700 pictures per second, which was mounted on the impact hammer facing the specimen. Because of the high frame rate and the sensor size of the camera, two GSVitec Multiled MT 50 000 lm lights were used with the camera. The AOS M-VIT 4000 camera was triggered to record for a minimum shock of 10g and had a memory capable of a few seconds of footage. Besides the AOS M-VIT 4000 camera, a GoPro Hero 10 action camera was mounted in the debris corridor to record the impact at 240 frames per second. The location of the AOS M-VIT 4000 and GoPro Hero 10 cameras can be seen in Figure 2b. A Nikon D7100 camera was placed at the end of the corridor and was also used to document the broken pieces of the specimen post-impact.

The primary measurement of the tests was the position of the pendulum, pre- and post-impact. This was recorded with an analog Baumer EIL580P angular encoder with a resolution of approximately 0.005°, which corresponds to a positional resolution at the centre of the impact tip of over 0.5 mm. The Baumer EIL580P was mounted at the shear pin, and its position can be seen in Figure 2a.

To measure the peak impact force P_d in Equation (4), accelerometers were mounted on the impact hammer beside the impact hammer tip in Figure 8. The positions of the accelerometers are shown in Figure 2b. Because of the difficulty in estimating the peak impact force P_d in the design phase, 10g micro-electromechanical (MEMS) accelerometers were initially used. In theory, the 10g MEMS sensors could measure impact forces of up to 700 kN. The estimated static strength for the shortest specimens with the largest cross-sections was in the order of 120 kN. After testing a few of the weakest specimens, it was apparent that the capacity of the 10g MEMS sensors was insufficient. Therefore, 50g and 100g MEMS sensors were ordered, with the same results. It was believed that piezoelectric accelerometers would give better results, which led to the use of 100g and 250g piezoelectric accelerometers. The capacities of these accelerometers were occasionally exceeded, which is equivalent to forces of over 6 900 and 13 800 kN, respectively. Upon post-processing of the accelerometer data and the high-speed imagery, this data was deemed unfit for determining the peak impact force P_d. This is discussed in Section 4.

10g MEMS accelerometers were used to measure the dynamic elastic modulus E_d of each specimen. Two 10g MEMS accelerometers were mounted ±500 mm from the mid-span of the specimens, and non-destructive impact hammer tests at the mid-span were used to induce vibrations in the specimens. The vibration data was then processed to find the natural period T_n. Together with the mass m of the specimen, the natural period T_n was used to compute the dynamic elastic modulus E_d.

A linear variable differential transformer (LVDT) was also used with a manual hand-crane and weights to conduct static three-point bending tests to find the static elastic modulus E_s. However, the displacements from the LVDT resulted in inconsistent static elastic moduli E_s. Therefore, the dynamic elastic modulus E_d from the vibration-based method was used for all further processing of the data. A complete list of the cameras and sensors can be found in Cao et al. [29].

4 RESULTS

4.1 HIGH-SPEED CAMERA IMAGERY

Images from the AOS M-VIT 4000 high-speed camera of a typical failure process are shown in Figure 10. Initially, the impact hammer made initial flat contact with the specimen at its centre. During the initial contact, momentum was transferred to the specimen via shock loading. This is shown in Figure 10a. After the initial impact, a gap formed between the impact hammer and the specimen. The first crack always appeared on the tension side of the specimen, and often in the outermost lamella close to a material imperfection. The first crack often developed when there was no physical contact between the impact hammer and the specimen. This is shown in Figure 10b. Eventually, the impact hammer made contact with the specimen again and pushed through the specimen. During this time, the failure propagated from the tension side towards the compression side of the specimen. This is shown in Figure 10c.

https://doi.org/10.52202/069179-0002

The high-speed imagery was used to describe the impact process qualitatively and uncovered a clear bouncing behaviour of the specimen on the impact hammer. The imagery enabled the classification of the failures into five different failure modes and the determination of the time to failure of each specimen [28,29].

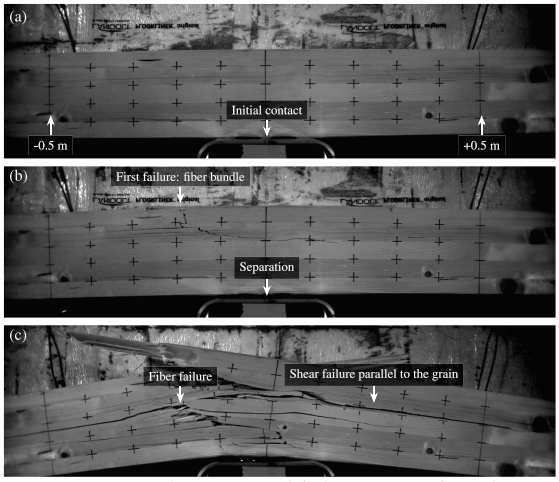

Figure 10: *Typical imagery and failure process from the AOS M-VIT 4000 high-speed camera with (a) initial contact between the impact hammer and the specimen at t=0 ms; (b) bouncing of the specimen with a gap forming between the impact hammer and the specimen at t=3.8 ms; and (c) full failure of the specimen with several failures at t=19.6 ms. The images are from tests on specimen 160×200×3600-F-4. The figure is reproduced from Cao et al.* [27,28]

4.2 SENSOR DATA

Data from an accelerometer mounted on the impact hammer is shown in Figure 11. If the 1 ms RMS-signal is interpreted, the peak impact force P_d based on Equation (4) was about 3500 kN. Compared with the mean value bending strength of GL24h [30], the peak impact force P_d was over 85 times higher with this method. It is obvious that this is not physically possible. This method of finding the peak impact force P_d can be further disowned by comparing the acceleration time history in Figure 11 with the high-speed imagery in Figure 10. Between t=3.0 ms and t=5.8 ms, there was no contact between the impact hammer and the specimen. The peak accelerations were measured at around t=3.3 ms. Therefore, there was no contact between the impact hammer and the specimen when the peak accelerations were measured. Moreover, the impact could not be characterised as perfectly inelastic based on imagery from the high-speed camera. Therefore, Newton's second law in Equation (4) cannot be used to compute the peak impact force P_d in such tests. The periodicity of the raw signal $|A|$ in Figure 11 corresponds to the natural period T_n of the impact hammer itself. The RMS accelerometer signal corresponded well to the observed bouncing of the specimen [26].

Figure 12 shows the data from the Baumer EIL580P angular encoder for specimen 160×200×3600-F-4. The release angle was 85.01°, which is equivalent to a potential energy mgh_0 of 146.7 kJ. The post-impact energy was measured after the pendulum impact hammer had completed a full cycle, coming back to the side of

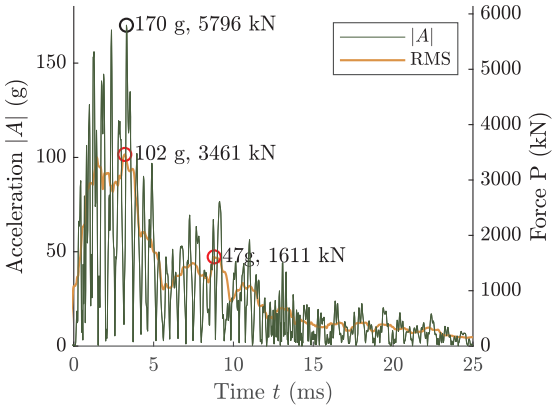

Figure 11: *Absolute values of the acceleration time history and the gliding 1 ms RMS signal for specimen 160×200×3600-F-4 from an accelerometer mounted on the impact hammer. The figure is adapted from Cao et al.* [27]

initial release. For the data shown in Figure 12, the post-impact angle was 80.32°, or 133.6 kJ. Because of the initial energy release from the electromechanical release system in Figure 9, the energy release during this cycle was corrected for by using data from free swing tests. By comparing the difference in potential energy mgh or the measured angles θ of the amplitudes following the impact hammer release for free swing conditions, the energy release E_r could be corrected for the release mechanism. Besides corrections for the release mechanism, corrections were also conducted for the intrinsic system damping by comparing free swing amplitudes with testing amplitudes, as well as the kinetic energy E_k from the propulsion of the broken halves of the specimens. This was done with the modal approximation technique [31].

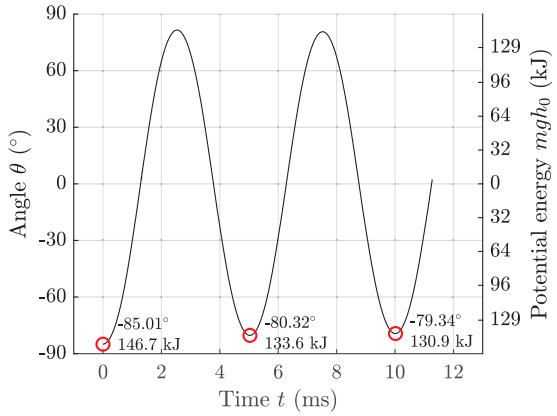

Figure 12: *Angular encoder data for specimen 160×200×3600-F-4.*

In Figure 12, the uncorrected difference between the initial and the first return peak was 4.69°, or 13.1 kJ. After corrections, the energy release E_r was $\Delta\theta$=3.22°, or E_r=8.99 kJ. The full results are presented in the test report [27]. By normalising the energy release E_r by the cross-sectional area, the toughness U_T can be found. For specimen 160×200×3600-F-4, the toughness U_T was 281 kJ/m^2.

https://doi.org/10.52202/069179-0002

5 CONCLUSION & OUTLOOK

In this paper, a pendulum impact hammer setup for impact testing of full-size timber beams was presented. The impact hammer was designed using computer-aided-design, and had a mass of 3450 kg, an effective length of 4750 mm, and could be released from a near-horizontal position. It was designed to accommodate simply supported timber beam specimens with and without axial restraints for cross-sections between 160×160 mm and 200×320 mm, and lengths between 2700 mm and 4300 mm. The main data from the tests was the energy release of the specimen throughout the impact, which was measured directly by the position of the impact hammer. The position of the impact hammer was recorded with an angular encoder. Besides the angular encoder, a shock-resistant high-speed camera operating at 5700 pictures per second was mounted on the impact hammer, and other cameras were also used to record the impact from several angles. Several accelerometers were also mounted on the impact hammer to measure the peak impact force. To date, 89 spruce glued laminated timber specimens without finger joints, nine beech laminated veneer lumber specimens, and four calibration specimens were tested.

Throughout the current experimental campaign, the test setup worked reliably at a high success-rate. Based on the current results, it is not recommended to measure the peak impact force by using accelerometers mounted at the impact hammer. For future tests, it is planned to measure the reaction forces at the supports directly via load cells. To extend the current knowledge on the behaviour of glued laminated timber subjected to impact loading, tests are also planned for specimens with finger joints. The pendulum impact hammer can also be used for impact tests of other materials with little or no modification.

ACKNOWLEDGEMENT

The authors would like to thank Roth Burgdorf AG and Pollmeier Massivholz GmbH & Co. KG for their contributions to the project. In addition, the authors remain thankful for the assistance and support provided by the Bauhalle team at ETH Zurich. This article is part of the project *Robustness of tall timber buildings* at ETH Zurich and is generously funded by the Albert-Lück Stiftung.

REFERENCES

[1] Ramage MH, Burridge H, Busse-Wicher M, Fereday G, Reynolds T, Shah DU, et al. The wood from the trees: The use of timber in construction. Renewable and Sustainable Energy Reviews 2017;68:333–59. https://doi.org/10.1016/j.rser.2016.09.107.

[2] Crews KI. Nonconventional timber construction. Nonconventional and Vernacular Construction Materials: Characterisation, Properties and Applications 2020:437–66. https://doi.org/10.1016/B978-0-08-102704-2.00016-0.

[3] Mpidi Bita H, Huber JAJ, Palma P, Tannert T. Prevention of Disproportionate Collapse for Multistory Mass Timber Buildings: Review of Current Practices and Recent Research. Journal of Structural Engineering 2022;148. https://doi.org/10.1061/(asce)st.1943-541x.0003377.

[4] Huber JAJ, Ekevad M, Girhammar UA, Berg S. Structural robustness and timber buildings–a review. Wood Mater Sci Eng 2019;14:107–28. https://doi.org/10.1080/17480272.2018.1446052.

[5] Voulpiotis K, Schär S, Frangi A. Quantifying robustness in tall timber buildings: A case study. Eng Struct 2022;265:114427. https://doi.org/10.1016/J.ENGSTRUCT.2022.114427.

[6] Cao AS, Grönquist P, Frangi A. Manuscript under peer review: Catenary action in strip-reinforced wood and timber beams. Constr Build Mater 2023.

[7] Cao AS, Palma P, Frangi A. Column removal analyses of timber structures - Framework to assess dynamic amplification factors for simplified structural design methods. World Conference on Timber Engineering 2021, WCTE 2021, Santiago, Chile: 2021, p. 1717–24.

[8] Svatoš-Ražnjević H, Orozco L, Menges A. Advanced Timber Construction Industry: A Review of 350 Multi-Storey Timber Projects from 2000–2021. Buildings 2022;12:404. https://doi.org/10.3390/buildings12040404.

[9] Binck C, Cao AS, Frangi A. Lateral stiffening systems for tall timber buildings–tube-in-tube systems. Wood Mater Sci Eng 2022. https://doi.org/10.1080/17480272.2022.2086066.

[10] Cao AS, Stamatopoulos H. A theoretical study of the dynamic response of planar timber frames with semi-rigid moment-resisting connections subjected to wind loads. Eng Struct 2021;240. https://doi.org/https://doi.org/10.1016/j.engstruct.2021.112367.

[11] Vilguts A, Malo KA, Stamatopoulos H. Moment resisting frames and connections using threaded rods in beam-to-column timber joints. WCTE 2018 - World Conference on Timber Engineering 2018:1–8.

[12] Johansson M, Linderholt A, Jarnerö K, Landel P. Tall timber buildings - A preliminary study of wind-induced vibrations of a 22-storey building. WCTE 2016 - World Conference on Timber Engineering 2016.

[13] Rebouças AS, Mehdipour Z, Branco JM, Lourenço PB. Ductile Moment-Resisting Timber Connections: A Review. Buildings 2022;12:240. https://doi.org/10.3390/buildings12020240.

[14] Cao AS, Frangi A. Mixed Element Method for Progressive Collapse Analysis: Method Description and Verification. In: di Trapani F, editor. Proceedings of Eurasian OpenSees Days 2022, Torino, Italy: Springer Nature; 2022.

[15] Adam JM, Parisi F, Sagaseta J, Lu X. Research and practice on progressive collapse and robustness of building structures in the 21st century. Eng Struct 2018;173:122–49. https://doi.org/10.1016/j.engstruct.2018.06.082.

[16] Baumann G, Brandner R, Müller U, Stadlmann A, Feist F. A Comparative Study on the Temperature Effect of Solid Birch Wood and Solid Beech Wood

under Impact Loading. Materials 2021;14. https://doi.org/10.3390/ma14247616.
[17]Pinto Moreira A, da Silveira E, Henrique de Almeida D, Hendrigo de Almeida T, Hallak Panzera T, Luís Christoforo A, et al. Toughness and Impact Strength in Dynamic Bending of Wood as a Function of the Modulus of Elasticity and the Strength in Compression to the Grain. International Journal of Materials Engineering 2017;7:61–7. https://doi.org/10.5923/j.ijme.20170704.01.
[18]Bučar DG, Merhar M. Impact and dynamic bending strength determination of Norway spruce by impact pendulum deceleration. Bioresources 2015;10:4740–50. https://doi.org/10.15376/biores.10.3.4740-4750.
[19]Widmann R, Steiger R. Impact loaded structural timber elements made from Swiss grown Norway spruce. In: Görlacher R, editor. CIB-W18 Meeting Forty-Two. International council for research and innovation in building and construction. Working commission W18 - timber structures., Dübendorf, Switzerland: Universität Karlsruhe; 2009, p. 1–11.
[20]Leijten AJM. Impact crash and simulation of timber beams. Transactions on Modelling and Simulation, vol. 30, Tallinn, Estonia: 2001, p. 859–68. https://doi.org/10.2495/CMEM010841.
[21]Jansson B. Impact Loading of Timber Beams. Master Thesis 1992. https://doi.org/10.14288/1.0050473.
[22]Blank L, Fink G, Jockwer R, Frangi A. Quasi-brittle fracture and size effect of glued laminated timber beams. European Journal of Wood and Wood Products 2017;75:667–81. https://doi.org/10.1007/s00107-017-1156-0.
[23]Madsen B, Buchanan AH. Size effects in timber explained by a modified weakest link theory. Canadian Journal of Civil Engineering 1985;13:218–32. https://doi.org/10.1139/l86-030.
[24]European Committee for Standardization. EN 1995-1-1:2004. Eurocode 5: Design of timber structures - Part 1-1: General - Common rules and rules for buildings. Brussels, Belgium: 2004.
[25]Schweizerische Ingenieur- und Architektverein. SIA 265. Zurich: 2021.
[26]Cao AS, Lolli M, Frangi A. Pendulum impact hammer tests on spruce GLT – Preliminary results. In: Topping BHV, Kruis J, editors. Proceedings of the Fourteenth International Conference on Computational Structures Technology, Edinburgh, UK: Civil-Comp Press; 2022, p. 1–8.
[27]Cao AS, Houen M, Lolli M, Frangi A. Pendulum impact hammer tests on glued laminated timber beams. Report 2022-01. Zurich, Switzerland: 2022. https://doi.org/10.3929/ethz-b-000585619.
[28]Cao AS, Houen M, Frangi A. Manuscript under peer review: Impact loading of glued laminated timber beams. Comput Struct 2023.
[29]Cao AS, Houen MT, Lolli M, Frangi A. Pendulum Impact Hammer Tests on Glued Laminated Timber Beams. Zurich: 2022. https://doi.org/10.3929/ethz-b-000585619.
[30]Schilling S, Palma P, Steiger R, Frangi A. Probabilistic description of the mechanical properties of glued laminated timber made from softwood. In: Görlacher R, editor. International Network on Timber Engineering Research, INTER: Proceedings, Meeting 54, 16-19 August 2021, Online, Timber Scientific Publishing, KIT Holzbau und Baukonstruktionen; 2021, p. 1–16.
[31]Martin JB, Symonds PS. Mode approximations for impulsively loaded rigid structures. 1965.

https://doi.org/10.52202/069179-0002